RESEARCH ARTICLE

Quantifying false bottoms and under-ice meltwater layers beneath Arctic summer sea ice with fine-scale observations

Madison M. Smith[1],*, Luisa von Albedyll[2], Ian A. Raphael[3], Benjamin A. Lange[4], Ilkka Matero[2,5], Evgenii Salganik[6], Melinda A. Webster[7], Mats A. Granskog[4], Allison Fong[2], Ruibo Lei[8], and Bonnie Light[1]

During the Arctic melt season, relatively fresh meltwater layers can accumulate under sea ice as a result of snow and ice melt, far from terrestrial freshwater inputs. Such under-ice meltwater layers, sometimes referred to as under-ice melt ponds, have been suggested to play a role in the summer sea ice mass balance both by isolating the sea ice from saltier water below, and by driving formation of 'false bottoms' below the sea ice. Such layers form at the interface of the fresher under-ice layer and the colder, saltier seawater below. During the Multidisciplinary drifting Observatory for the Study of the Arctic Climate (MOSAiC) expedition in the Central Arctic, we observed the presence of under-ice meltwater layers and false bottoms throughout July 2020 at primarily first-year ice locations. Here, we examine the distribution, prevalence, and drivers of under-ice ponds and the resulting false bottoms during this period. The average thickness of observed false bottoms and freshwater equivalent of under-ice meltwater layers was 0.08 m, with false bottom ice comprised of 74–87% FYI melt and 13–26% snow melt. Additionally, we explore these results using a 1D model to understand the role of dynamic influences on decoupling the ice from the seawater below. The model comparison suggests that the ice-ocean friction velocity was likely exceptionally low, with implications for air-ice-ocean momentum transfer. Overall, the prevalence of false bottoms was similar to or higher than noted during other observational campaigns, indicating that these features may in fact be common in the Arctic during the melt season. These results have implications for the broader ice-ocean system, as under-ice meltwater layers and false bottoms provide a source of ice growth during the melt season, potentially reduce fluxes between the ice and the ocean, isolate sea ice primary producers from pelagic nutrient sources, and may alter light transmission to the ocean below.

1. Introduction

During the Arctic summer, rapid melt of snow and sea ice lead to large local sources of relatively fresh meltwater.

[1] Polar Science Center, Applied Physics Laboratory, University of Washington, Seattle, WA, USA

[2] Alfred Wegener Institute, Helmholtz Centre for Polar and Marine Research, Bremerhaven, Germany

[3] Thayer School of Engineering, Dartmouth College, Hanover, NH, USA

[4] Norwegian Polar Institute, Fram Centre, Tromsø, Norway

[5] Svalbard Integrated Arctic Earth Observing System Knowledge Centre, Longyearbyen, Svalbard, Norway

[6] Norwegian University of Science and Technology, Trondheim, Norway

[7] University of Alaska Fairbanks, Fairbanks, AK, USA

[8] Key Laboratory for Polar Science of the MNR, Polar Research Institute of China, Shanghai, China

* Corresponding author:
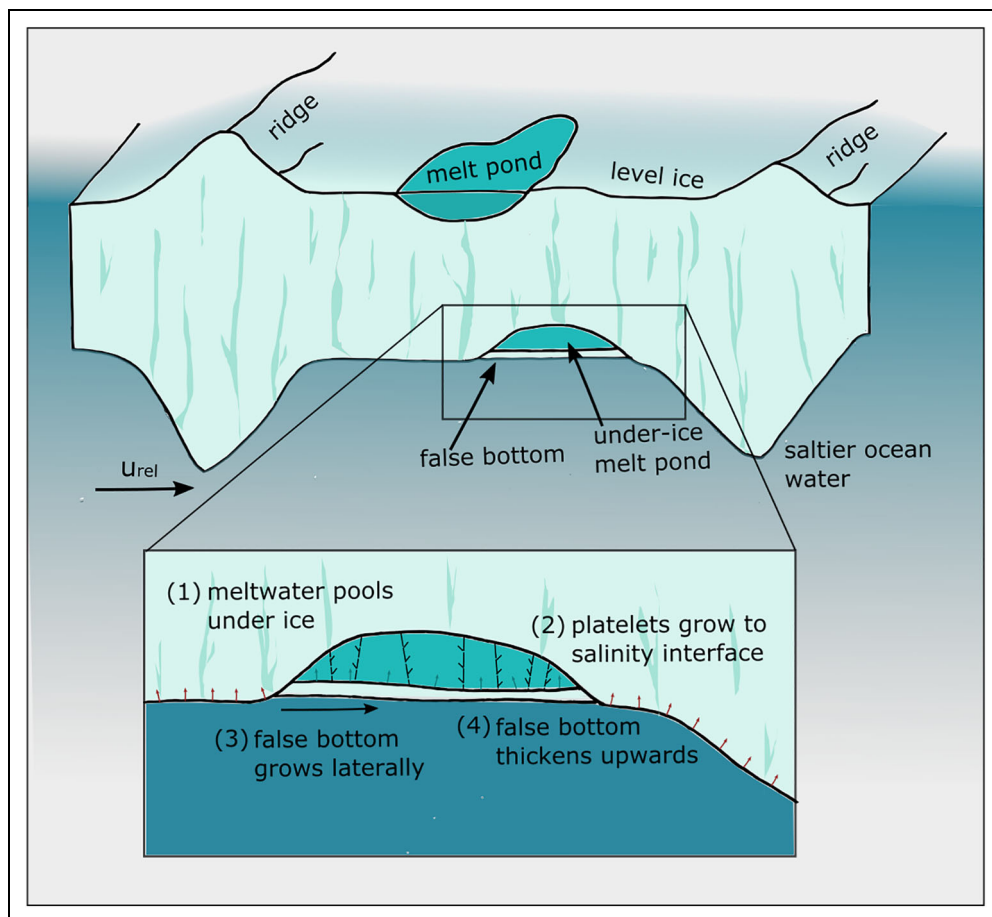Email: mmsmith@apl.washington.edu

While some of this meltwater accumulates in melt ponds on the sea ice surface, the majority drains to the ocean (Eicken et al., 2002; Perovich et al., 2021), either vertically through the ice or laterally over the ice to open water leads. The fresher, less dense water remains on top of the denser, saltier water below. In calm ocean conditions, this meltwater can be pooled beneath ice floes in under-ice meltwater layers (**Figure 1**), sometimes referred to as under-ice melt ponds (Hanson, 1965). Mixing in the upper ocean can result in this meltwater being entrained into the mixed layer, contributing to freshening.

Under-ice meltwater layers have been observed sporadically in the Arctic basin since Fridtjof Nansen's 1893–1896 expedition (Nansen, 1902), typically under ice that is thin or with topographic depressions (Eicken, 1994). Expeditions since then in multiyear ice have indicated that these features are typically found in June–July, during the peak of summer melt (e.g., Eicken, 1994; Perovich et al., 2003; Lange et al., 2021). One such under-ice meltwater

Figure 1. Schematic of under-ice meltwater layers and false bottom formation. Wadhams et al. (2006) described how surface melt ponds often correspond with bottom depressions, such that the bottom topography mirrors the surface topography. This mirror effect is likely a result of preferential absorption of solar energy in surface melt ponds, which results in an enhanced local heat flux to melt the bottom of the ice (Taylor and Feltham, 2004). Martin and Kauffman (1974) described the formation of false bottoms beginning with the pooling of relatively fresh meltwater in depressions, which initially grows platelet ice. False bottoms (with thickness on order of centimeters) then grow laterally from the ice (with thickness on order of meters) which serves as an anchor point. False bottoms then thicken upwards towards the ice bottom. This process is dependent on the relative ice–ocean velocity, u_{rel}.

layer was sampled extensively during a field campaign in multiyear ice in the Central Arctic (Eicken, 1994). Observations of this meltwater layer showed that it contained water primarily from precipitation (i.e., snowmelt). Ice core analysis showed that the meltwater layer modified the properties of the overlying multiyear ice through diffusional desalinization. While direct observations of under-ice melt ponds are relatively sparse, the frequency of their observed effect on ice cores (Eicken, 1994; Lange et al., 2021) suggests that these features may be common.

Freezing at the salinity interface between under-ice meltwater layers and the underlying seawater can result in the formation of 'false bottoms' (Martin and Kauffman, 1974), contributing to the summer sea ice mass balance. False bottom formation is a result of double-diffusion processes at the boundary between freshwater and saltwater when both are at the freezing point, where the rapid diffusion of heat from freshwater to saltwater relative to salt results in a density inversion and high Rayleigh number convection. Martin and Kauffman (1974) described

this process with laboratory studies, summarized schematically in **Figure 1**. Initially, supercooling results in the growth of platelet sheets down from the ice floe bottom to the salinity interface. Then, false bottom growth progresses from platelets laterally across the interface through diffusive processes. This lateral growth results in a water-filled void space between the false bottom and the ice above. Continued false bottom growth and thickening progresses upwards, towards the main floe. The resulting false bottom likely buffers the overlying ice against subsequent melt to some extent, but melting can still occur at the ice bottom from heat conduction through the floe surface even as false bottoms are forming below. When the meltwater layer temperature under the ice is higher than the freezing point, it may also create an upward heat flux and promote sea ice melting. In fact, warming of under-ice meltwater layers may sometimes lead to preferential melt in low-draft areas, in contrast to the conventional wisdom that the thickest ice melts fastest during summer (e.g., Wadhams, 2000).

Previously, there had been a number of anecdotal observations of false bottom formation in under-ice meltwater layers (e.g. Untersteiner and Badgley, 1958; Hanson, 1965), with thicknesses in the range of 2–10 cm. A more systematic evaluation of false bottom formation was provided by the year-long SHEBA observational campaign in the western Arctic, where false bottom formation was observed at about 15% of mass balance stakes in the summer of 1998 (Perovich et al., 2003). Their presence was short-lived (less than a week) and tended to be under thinner, heavily-ponded ice. Despite the relatively low concentration of under-ice layers and false bottoms, they are likely a significant component of the net summer ice mass balance (Eicken et al., 2002). Comparison of autonomous buoy observations from two nearby sites in the high Arctic during the 2013 melt season showed that a transient under-ice meltwater layer and subsequent false bottom formation at one location resulted in approximately 0.5-m thicker ice entering the refreeze period (Provost et al., 2019). False bottoms have also been indicated by observations in coastal regions with more freshwater contribution from runoff (Wang et al., 2013).

Process modeling can provide insight on the physical drivers of these small-scale features. Notz et al. (2003) presented an analytical model describing the formation and evolution of this layer through diffusional transport. Using a simplified forcing time series, the model is able to generally capture observed false bottom evolution during SHEBA (Perovich et al., 2003). This nonlinear process was modeled similarly by Alexandrov and Nizovtseva (2008). Smith (2019) built on these prior models to derive a model for the initial platelet crystal growth and lateral growth at the salinity interface. Smith (2019) also developed a model for formation and evolution in the context of a sea ice slab, whereas prior work modeled the false bottom in isolation. In this context, the model suggests that the local impact on mass balance may be significant, with an average of 5-cm greater sea ice thickness in the presence of false bottoms under typical Arctic conditions over a 50-day period. Although there is evidence suggesting that under-ice meltwater layers and false bottoms could be widespread in the Arctic (Eicken, 1994), no attempt has been made to model these features on the basin-scale as the vertical scale of these features and their topographic controls are not resolvable in most large-scale models.

Under-ice meltwater layers and false bottoms can have substantial impacts on many key processes in the sea ice system, in addition to the mass balance. The retention of meltwater in under-ice layers (estimated as 13% of total meltwater volume by Eicken et al., 2002) can result in delayed freshwater input to the mixed layer. However, the presence of the false bottom may result in freshening and shallowing of the mixed layer locally by blocking brine expulsion (Smith, 2019). There is likely a reduction in gas fluxes through the ice, both from the reduction in ice porosity with growth of the fresher ice layer and from the strong halocline acting as a barrier in the ocean. As Arctic sea ice algal communities typically have the highest biomass within the bottom few centimeters of the ice column

(Spindler, 1990; Gradinger, 1999; Lange et al., 2015), under-ice meltwater layers are likely to impact growth of these organisms and result in differences in community structure (Gradinger, 1996). False bottoms also concentrate and release suspended material by trapping compounds and organisms into the new ice matrix, which alter ecological interactions between microbes and their chemical environment. Gradinger (1996) characterized such different communities and showed that, while the bottom of the sea ice was largely inhabited by diatoms, the under ice meltwater layer was dominated by autotrophic flagellates. Additionally, the growth of relatively fresh ice with extinction coefficients greater than that of seawater (Perovich and Grenfell, 1981) and the presence of ocean layers that may increase scattering and absorption both likely act to decrease the transmitted light to the ocean below.

The year-long MOSAiC drift expedition (October 2019 to September 2020) in the Central Arctic based from the R/V *Polarstern* provided a unique opportunity to observe the timing and duration of under-ice meltwater layers and to analyze their occurrence in the context of the formation and deformation history of the ice (Shupe et al., 2020; Nicolaus et al., 2022). During this expedition, coordinated observations of the atmosphere-ice-ocean physical system were made alongside measurements of the ecosystem and biogeochemical processes. The presence of under-ice meltwater layers and false bottom formation was observed near the beginning of the melt season at a number of locations around the MOSAiC floe. In this paper, we examine the prevalence and distribution of these features, and their association with other factors, including ice thickness, ridges, melt ponds, wind speed, and drift speed. We then combine observations with 1D modeling to investigate the factors that drive the formation and persistence of under-ice meltwater layers and false bottoms. The results provide new insights for estimating the abundance of under-ice meltwater layers and false bottoms, and interpreting atmospheric, sea ice and near-surface oceanic and ecological time series measured on the MOSAiC floe.

2. Methods

Under-ice meltwater layers and false bottoms were observed during the MOSAiC expedition from June to July 2020 (Leg 4; Shupe et al., 2020; Nicolaus et al., 2022). Observations were made primarily over the "Central Observatory" (CO-2; Nicolaus et al., 2022), which was a floe with a circumference of about 3 km during this time. During the study period, the position of the floe was between 82.0°N, 8.3°E and 78.8°N, 2.3°W. The floe was characterized as a mix of first-year ice (FYI) and second-year ice (SYI). A part of this SYI was heavily deformed and was thicker than the ice within a general radius of 50 km (von Albedyll et al., 2022). A network of observatories and measurement sites were laid out across the floe, the full extent of which is described in Nicolaus et al. (2022); here we focus on describing the datasets used in our analysis and interpretation.
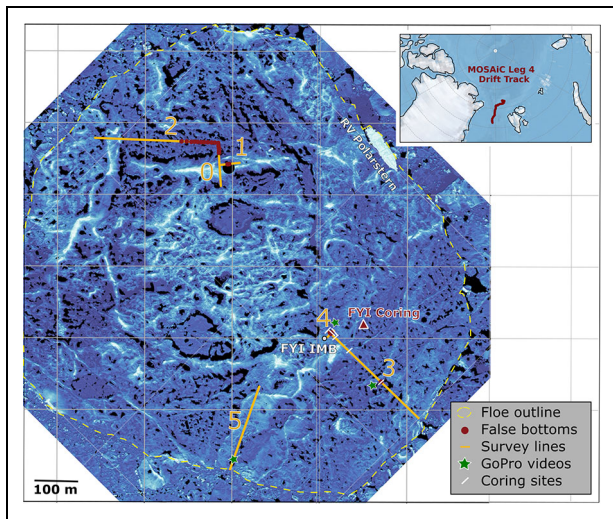
Figure 2. Map of survey line locations on the MOSAiC floe, July 2020. Yellow dashes outline the edge of the MOSAiC floe. Gold lines indicate survey lines where drilling was completed to check for false bottom presence, and dark red markers indicate where false bottoms were observed. FYI coring site (dark red triangle) and FYI Ice Mass Balance buoy (IMB) included in the analysis are labeled. Green stars indicate locations of GoPro videos. White hash marks indicate dedicated coring sites for isotope sampling. Blue color scale shows approximate freeboard elevation from the airborne laser scanner (ALS) surveys ranging from 0–1.4 m with lighter shades indicating higher freeboard values. Black areas indicate water surfaces where laser measurements cannot be retrieved, and thus are typically indicative of melt ponds. Inset in upper right shows the drift track of the MOSAiC CO from June 18 to August 1, 2020.

2.1. Survey lines

2.1.1. Observations of false bottoms

Following the initial identification of false bottoms at various sites, five opportunistic survey lines were measured sequentially with the primary aim of determining the prevalence and distribution of false bottoms across the floe (**Figure 2**). The five survey lines, with a total of 132 holes drilled, were measured over the period of July 14–29 (**Table 1**). These lines were selected to cross a representative range of sea ice types (FYI and SYI) and topographical variability, while avoiding disruption of other measurements and experiments. Holes were drilled with a 2-inch Kovacs sea ice auger. Distance to the sea ice bottom (void space top), false bottom top (void space bottom), and bottom of the false bottom were measured using a graduated rod with a hook on the bottom, allowing us to calculate the thickness of the sea ice, void space, and false bottom. A schematic of this measurement approach can be found in the dataset archive (Smith et al., 2021b). The typical sea ice thickness tape could not be used, as it did not allow for distinguishing between main ice floe and false bottom.

Observations where the measured 'false bottom' under the void space was thicker than 0.3 m were assumed to be a result of rafting rather than false bottom formation (7 locations; 5% of measurements). Ice characteristics at locations where this cutoff was applied qualitatively agreed with this interpretation (e.g., thicker ice in deformed areas, and thicker ice below the void space than would be expected to grow through false bottom formation). This rafted ice thickness is included in the total ice thickness.

2.1.2. Observations of under-ice meltwater layers

While we can infer that under-ice meltwater layers are present at all locations where false bottoms are observed, additional profiles of temperature and salinity beneath the ice were completed along transects over 5 days in a total of 36 holes with the aim of quantifying the characteristics of under-ice meltwater. These observations were completed at a subset of locations on the survey lines focused on false bottoms (**Figure 2**; **Table 1**). Based on the timing and location of sampling activities, we do not believe that the observed meltwater features were the direct result of prior sampling activities, such as drilling or coring. The observation of melt pond drainage on the floe scale at times other than when sampling occurred suggests that the sampling activities did not dramatically impact the evolution of meltwater that we hoped to observe.

Measurements were completed with a YSI Professional Plus probe measuring temperature and conductivity. The probe was deployed through holes shortly after drilling, and care was taken during drilling and measuring to minimize disturbance to the under-ice water structure (where some mixing associated with drilling is expected). No drainage through holes for sampling activities was visible, suggesting that the surface and under-ice water were already hydraulically connected. The sensor was held at each depth for at least three seconds, with continuous minor up and down motion to encourage flushing through the sensor. Conductivity was converted to practical salinity using PSS-78 by the instrument software, which includes a correction for temperature, and is unitless. The conductivity sensor was calibrated onboard using standard conductivity calibration fluid from YSI. Depth of the conductivity sensor was recorded manually using a measuring tape. Data processing included a correction for the 4-cm offset between temperature and conductivity sensors on the probe, which was done by calculating a separate set of depth values for the temperature measurements, and then linearly interpolating temperature data to the depth values of the salinity profiles.

Compared to traditional profiling, collection of point measurements to form a profile allowed adaptive sampling based on the features observed. The depth and spacing of profile measurements varied, but typically began at the sea ice bottom, and continued at a spacing of 3–5 cm until the salinity had stabilized near mixed layer values (typically around 2–4 m below the ice surface), which decreased over the month of July from approximately 33.8 to 32.0. Note that some measurements were made in the drill hole at depths where ice was present (e.g., **Figure 3**), but do not represent the temperature and

Table 1. Summary of survey lines of false bottom and under-ice meltwater layers

Date	Line	# FB[a]	# FWE[b]	FB %	FB Thickness (m)	FWE %	FWE Thickness (m)
July 14	0	16	5	44	0.08	40	0.13
July 16	0	5	2	20	0.10	40	0.04
July 16	1	3	3	0	0	67	0.07
July 19	2	23	15	43	0.08	27	0.06
July 25	3	34	0	12	0.06	na[c]	Na[c]
July 25	4	5	0	40	0.11	na[c]	na[c]
July 27	5	19	1	0	0	0	0
July 29	5	27	10	0	0	0	0

[a] Number of holes samples for false bottoms (FB).
[b] Number of holes sampled for freshwater equivalent (FWE).
[c] Not applicable.
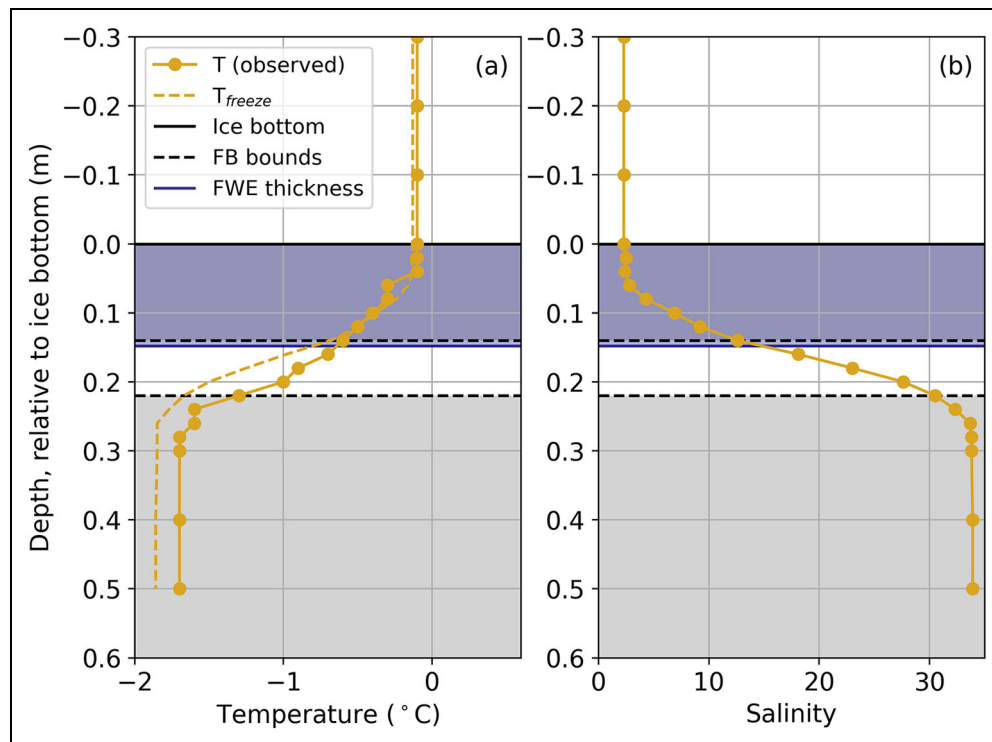
Figure 3. Example calculation of false bottom and FWE thickness. A profile from July 14, Line 0 position 5, demonstrates the calculation of false bottom (FB) and freshwater equivalent (FWE) layer thicknesses. Profiles of water temperature (left) and salinity (right) measured through the hole drilled in ice and false bottom, plotted relative to the depth of the ice bottom, were used to calculate the thickness of the equivalent freshwater in the meltwater layer by Equation 1 (FWE; shaded navy and denoted by the solid navy line), here 0.15 m. The false bottom, bounded by dashed black lines, was 0.08 m thick.

salinity of the ice itself. Full description of data collection and processing is included in the data archive (Smith et al., 2021a).

2.1.3. Salinity and stable oxygen isotope sampling
Coring and sampling were completed at six locations along lines 3 and 4 (white lines in **Figure 2**) on July 25 for measurement of salinity and stable oxygen isotopic composition to better understand the meltwater sources

for under-ice meltwater and false bottoms. Cores were collected using a 9-cm diameter Mark II coring system (Kovacs Enterprises, US), and ice samples were collected from the bottom 10 cm of the ice core in 5-cm increments (0–5 and 5–10 cm above the bottom) and from the false bottom ice. Samples of the under-ice meltwater layer and water from directly below the false bottom were collected using a peristaltic pump. In order to minimize contamination from coring activities, under-ice meltwater samples

from the meltwater layer in the void space between ice and false bottom were collected prior to coring through the false bottom. Surface melt pond water samples were collected by dipping plastic sample cups (rinsed with milliQ water) in the melt ponds where cores were collected, prior to ice coring. In total, ice samples were collected from six cores, five of which included false bottoms, and water samples were collected from four surface melt ponds, three under-ice meltwater layers, and seawater beneath false bottoms at four locations.

Ice samples were melted onboard the R/V *Polarstern*, and salinities of all water and ice samples were measured onboard using a calibrated YSI model 30 probe (with salinity given in PSS-78 scale, unitless). Vials for oxygen isotope composition were shipped to the Alfred Wegener Institute (AWI) ISOLAB Facility in Potsdam, Germany, where they were analyzed for stable water isotopes with Finnigan MAT Delta-S mass spectrometers using equilibration techniques. The oxygen isotope composition is given as per mil difference relative to VSMOW (‰, Vienna Standard Mean Ocean Water), with an internal 1σ error better than 0.1‰ for $\delta^{18}O$ (Meyer et al., 2000).

2.1.4. Under-ice videos

Under-ice videos were taken along the survey lines in a number of locations with a GoPro Hero 8. Larger holes were drilled with a Kovacs corer (9-cm internal diameter), and the camera was slowly lowered down through the hole and into the ocean below on a pole. Videos S1–S4 provided visual footage of false bottoms and the under-ice meltwater layers (distinguishable as a result of the refraction of light at the interface between fresher and saltier water). Additionally, a Blueye ROV was deployed through large holes at various research sites on the floe and through leads. Video recordings provide additional visual confirmation and insight on the characteristics, distribution, and impact of under-ice features.

2.2. Ancillary observations

The MOSAiC sea ice physics coring program included weekly collection and processing of a number of full thickness sea ice cores from dedicated level ice areas (Granskog, 2021). This effort included measurements of the sea ice thickness and freeboard, and profiles of ice temperature and salinity. False bottoms were observed at the FYI coring site, but were absent at the second-year ice (SYI) coring site. Time evolution of the FYI coring site false bottom thickness (Table S1) are used here to supplement survey line observations.

In addition, profiles of upper ocean temperature from an ice mass balance buoy (IMB) installed near the FYI coring site (2019T66) provide insight into the temporal evolution of meltwater in under-ice layers (Lei et al., 2021). A thermistor chain frozen into the ice measured temperature every 6 hours to approximately 5 m below the ice surface at a spacing interval of 2 cm. Once a day, the thermistor chain underwent a heating cycle, and temperatures recorded 30 and 120 seconds after the end of the heating were used to identify the sea ice bottom qualitatively. Temperature below the sea ice was used to

calculate salinity for the period of interest by assuming all water was at the freezing point temperature. Our YSI profile observations indicate that this assumption is reasonable, as temperatures were usually within a few tenths of a degree of freezing (e.g., **Figure 3**), but may have underestimated salinity when water was actually above the freezing temperature. Values shown here are averaged to daily values (24-hour).

Wind and drift speed were calculated using measurements from the ship-based meteorological observatory, which provided the most continuous time series during ship operation (Schmithüsen, 2021). Measurements were combined from various instruments on the vessel, corrected for instrument height above sea level, and subjected to complete quality control. The 1-minute averages provided in the full data set were averaged here to daily values (24-hour). Wind speed was measured using a Thies Clima 2D Ultrasonic Anemometer, and drift was based on the GPS values which provide the instantaneous drift speed of the ship as it was attached to the MOSAiC floe.

2.3. Calculation of freshwater content

The freshwater content of under-ice layers was calculated as the 1-dimensional freshwater equivalent (FWE; example in **Figure 3**) that accounts for the salinity profile observed beneath the ice:

$$FWE = \int_{z(S=S_{ref})}^{z=icebot.} (1 - \frac{S}{S_{ref}})dz \qquad (1)$$

where S is the measured salinity profile, S_{ref} is a reference far field salinity determined using the salinities observed at the bottom of profiles on each date (typically 31–34), and the reference salinity depth ($z(S = S_{ref})$) is the shallowest depth at which this salinity was observed. This equation gives the equivalent thickness (relative depth) of water with a practical salinity of 0 necessary to account for the freshwater between the ice bottom and reference salinity depth. This relative depth then typically corresponds to a depth of intermediate salinity, between the endpoints of 0 and S_{ref}. This approach was applied to the IMB profiles in the same manner as the YSI profiles, with the exception that the salinity profiles for the IMB measurements were inferred by assuming freezing temperature, rather than directly measured salinity.

Equation (1) was used to provide quantification of under-ice meltwater layer thickness that is distinct from the presence and thickness of false bottoms. We hypothesize that under-ice meltwater layers correspond to false bottom locations and that the thickness of this layer plays a role in the thickness of the void space between the main ice and the false bottom, as well as the thickness of the false bottom that may form. However, there are many scenarios where an under-ice meltwater layer may be present in absence of a false bottom or where the thickness of the layer may be greater or less than the distance to the bottom of the false bottom itself. Thus, we chose to ignore the salinity of the false bottom itself in calculating under-ice FWE.

We considered an under-ice meltwater layer to be present when the equivalent freshwater thickness FWE was greater
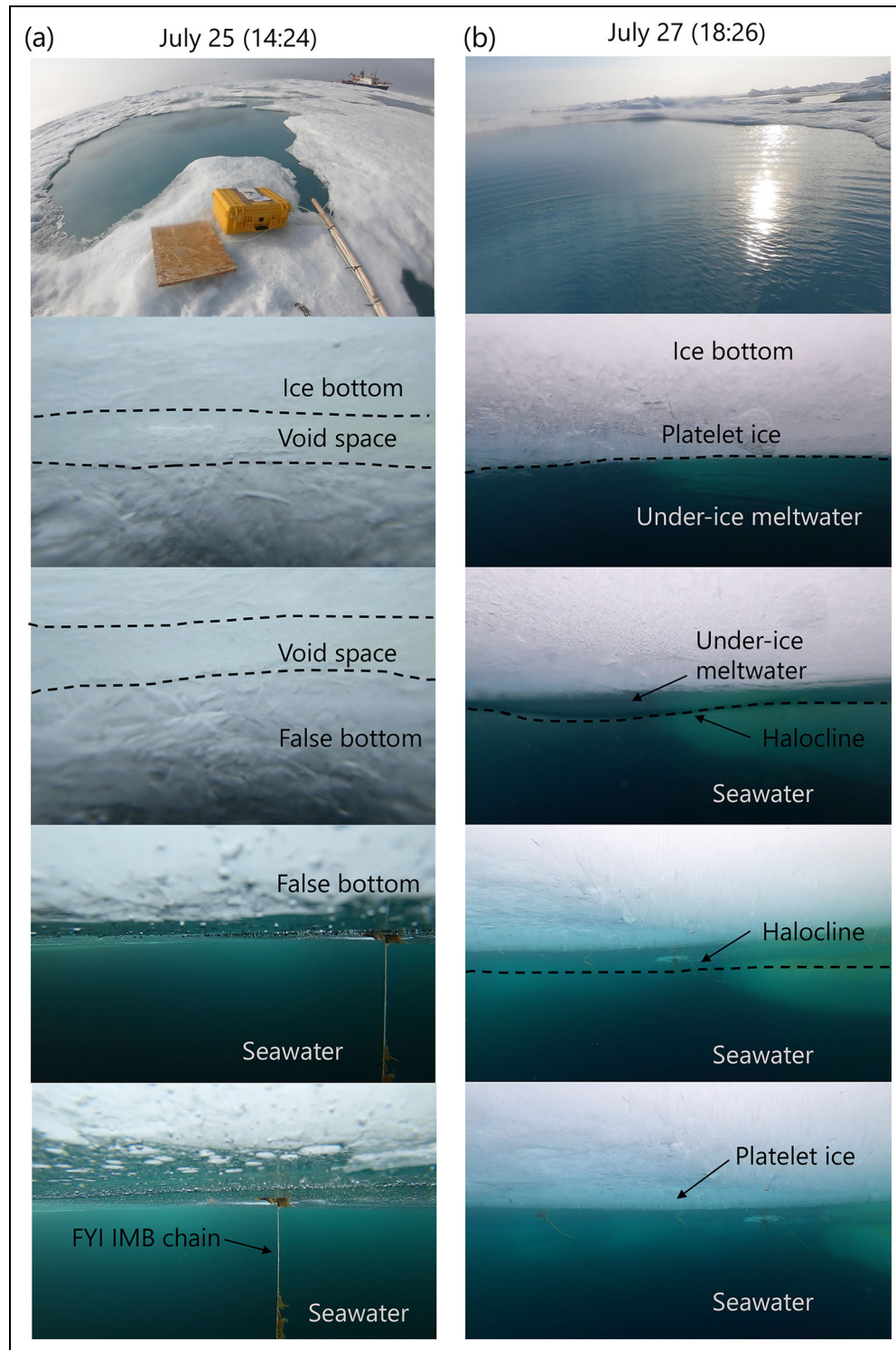
Figure 4. Screenshots of under-ice features from GoPro profiles. Still images from GoPro videos (a) on July 25, showing a false bottom under survey Line 4, and (b) on July 27, showing an under-ice meltwater layer and platelet ice on Line 5. The image sequences show the downwards progression through the ice and water column from top to bottom with key features annotated, and the first row of images showing the ice surface at each location. Full GoPro videos are available as Video S1 and Video S4.

than 0.02 m. We excluded all observations of rafted ice from the analysis, which can otherwise erroneously affect the interpretation of the time series of the equivalent freshwater thickness. Although the trapping of meltwater between rafted floes may be interesting for different reasons, it is unlikely to result in the formation of false bottoms.

3. Results and discussion

GoPro videos taken along survey lines 4 and 5 on July 25 and 27, respectively, provided visual confirmation of freshwater layers and false bottoms and context for the conditions in which they occurred. **Figure 4** shows still images from these videos (progressing downwards from top to

bottom) of a false bottom (a) and an under-ice meltwater layer (b). The locations of these videos are indicated by the green stars on the map (**Figure 2**). Clearly visible is the transition from the main sea ice floe to the false bottom as delineated by the void space, but the false bottom is characterized by a very loose structure, with platelets extending upwards into the void space. The bottom of the false bottom appears smooth and glassy, similar to that described in the experiments of Martin and Kauffman (1974). The halocline at the boundary between under-ice meltwater and the ocean below can be seen in the videos as a shimmer when passing through, and as a reflective surface when viewed from below.

Here we characterize both the spatial and temporal occurrence of under-ice meltwater layers and false bottoms and the factors driving their distribution. We can identify a number of conditions that are necessary to form under-ice meltwater layers, which may subsequently result in growth of false bottoms:

1. An input of fresher water is needed. This input occurs throughout the summer from snow and sea ice melt. Meltwater drainage happens both gradually through the ice, and can also occur in more rapid drainage events.
2. The under-ice topography needs to be conducive to accumulation of the meltwater. This accumulation occurs in topographic lows in the ice basal surface with relatively small draft, and is likely related to the proximity and spacing of topographical ridges and their under-ice keels, which provide a shelter and barrier to trap water between.
3. Mixing needs to be sufficiently low for the meltwater to remain stratified as an under-ice layer, rather than being entrained into the deeper mixed layer. Specifically, turbulence must be low enough so that the existing stratification from freshwater input and upper ocean warming is not overcome. The turbulence is expected to be strongly related to the wind and sea ice drift speed, which drive mixing.

Condition 2 (topography) is primarily a spatial control on variability such that it remains relatively constant over the relevant time period, while the first and third conditions can evolve over time. The details of these factors are discussed alongside the observations in subsections focusing on spatial and temporal distribution.

3.1. Spatial distribution

Histograms of the ice thicknesses at all observation points and where features were observed show that both false bottoms and under-ice meltwater layers are most likely to occur under relatively thin ice, with thicknesses of 0.5–1.7 m (**Figure 5**). The exclusion of rafted ice areas from classification as under-ice meltwater layers removed two points along on Line 1. Most false bottoms occurred under ice with a thickness of 1.0–1.3 m, and 60% of ice observed in this thickness range had false bottoms
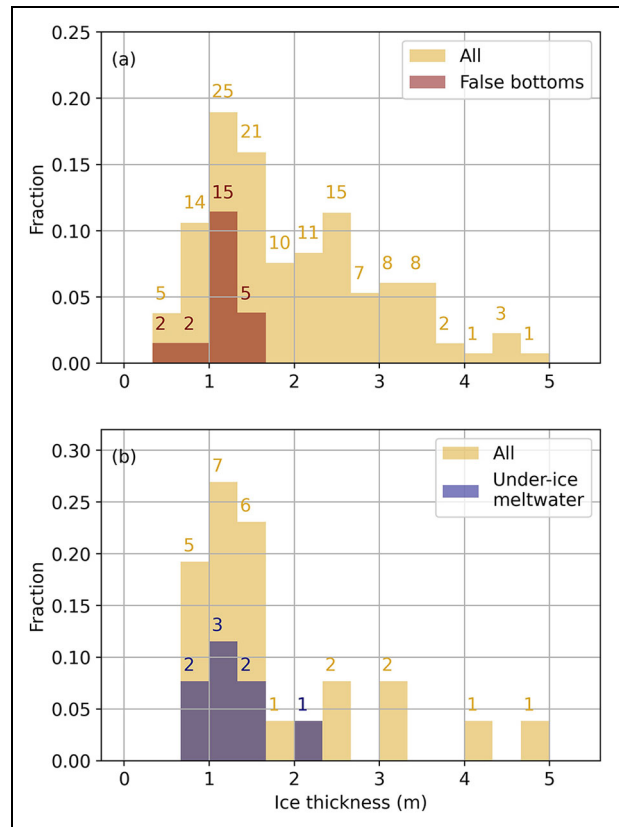

Figure 5. Relative fraction of ice thicknesses where false bottoms and under-ice meltwater layers were observed. Normalized histogram of all ice thicknesses (in gold) along survey lines for (a) false bottoms and (b) under-ice meltwater layers. Ice thicknesses of observations that contained false bottoms (in dark red) and under-ice meltwater (in navy) are overlain as the relative fraction of all observations. Numbers on top of the bars indicate the total number of samples in each bin. While under-ice meltwater layers have been inferred where false bottoms are observed, the specific temperature and salinity structure was only observed at select locations.

present. The majority of these false bottoms were observed along Lines 0 and 2 (**Figure 2**; **Table 1**).

Qualitatively, we observed that false bottoms occurred under ice that was level (**Figure 2**). However, not all thin, level ice had under-ice meltwater layers or false bottoms, and under-ice meltwater layers did not necessarily correspond spatially with surface melt pond extent (**Figure 1**). This spatial variability is a result of the additional impact of topography, where ridges help confine meltwater layers and provide anchoring points for false bottom layers. Looking at the topography along Line 2 in more detail (**Figure 6**) shows that the surface ridge corresponds to a subsurface feature around 120 m constraining the extent of under-ice meltwater layers and false bottoms. However, to understand why under-ice features are not observed in areas on both sides of this keel, we must look at the 3-dimensional topographical differences.
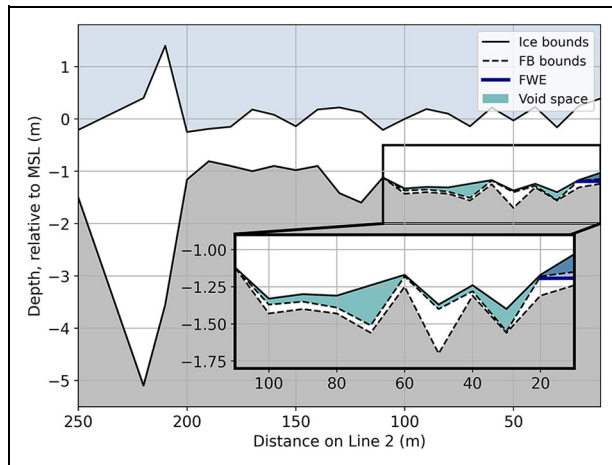
Figure 6. Topography from drill line survey along Line 2 on July 19. False bottom (FB; bounds shown as dashed black lines) is observed below the main ice floe (solid black lines) from 10–110 m (see inset), and the void space between is shown with teal shading. The navy line shows the location of the under-ice meltwater layer surface in terms of equivalent freshwater (FWE) below the ice bottom, where applicable (0–20 m). Depths shown relative to mean sea level (MSL).

Freeboard maps from airborne laser scanner (ALS) surveys allowed us to explore in more detail the role of topography in the spatial distribution of these features (**Figure 7**); although the sub-surface topography is not directly indicated by the observed surface topography, there is a strong correlation between the two (Wadhams, 1981). The most striking difference between the area without false bottoms (approximately 140–200 m in **Figure 6**) and where false bottoms were observed (dashed line in **Figure 6**) is the absence of ridges encircling it. The blue lines (**Figure 7**), which delineate the 0.2-m contour, highlight the presence of ridges. The area in red (**Figure 7**) is proximal to two ridges (suggested by freeboard greater than 0.2 m), while the other area has only one ridge bordering it. This result is consistent with prior work suggesting that ice keels can help trap shallow freshwater layers when they are moving at a speed similar to that of the ice (Skyllingstad et al., 2003). Based on this analysis, we conclude that factors controlling the spatial distribution of false bottoms include relatively level ice with low freeboard and ridges that enclose low freeboard area on multiple sides. Here, false bottoms generally occur in areas with freeboard less than 0.1 m that are enclosed by ridges with freeboard greater than 0.2 m, but the specific values are likely to vary across floes.

3.2. Temporal evolution

Figure 8 summarizes the temporal evolution of features in survey line observations. Because the different survey lines were visited on different days (**Table 1**), some spatial variability is likely captured here, in addition to the temporal variability. Full plots of survey line observations on each date are provided in Figures S2–S9).
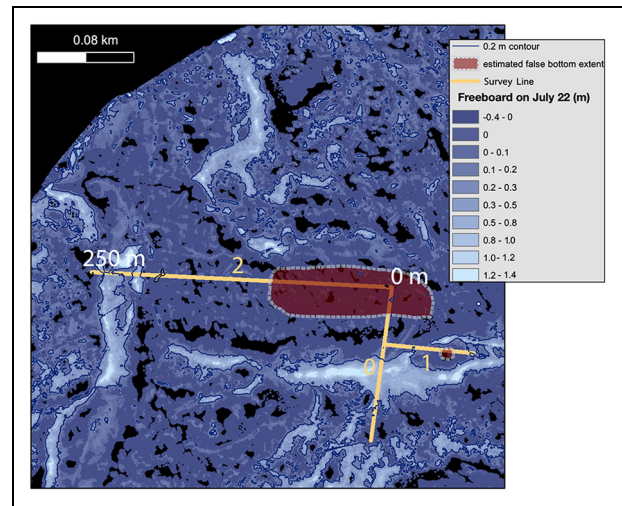

Figure 7. Map of sea ice freeboard from airborne laser scanner survey on July 22. ALS map (ALS quicklook, credits: Hendricks, von Albedyll, Birnbaum; data: Hutter et al., 2021) is zoomed into the area surrounding survey lines 0, 1, and 2. Red shading delineates the approximate area where we expect false bottoms were present based on the observations of false bottoms on July 16 (lines 0 and 1) and 19 (line 2) (**Figure 2**). Black areas indicate water surfaces where laser measurements are not retrievable, and thus are typically indicative of melt ponds. Blue lines indicate the 0.2-m contour.

Generally, a reduction in the occurrence of under-ice meltwater and false bottoms was observed over time throughout July (**Figure 8a**). The occurrence of false bottoms in some of the early observations is remarkably high, with 44% maximum occurrence frequency on July 14 and 19. The prevalence of under-ice meltwater and false bottoms are comparable, suggesting that false bottoms are likely to occur when under-ice meltwater layers are present.

Along survey lines, under-ice meltwater layers, when present, ranged from 0.04–0.13 m in average FWE thickness under the bottom of the ice (**Figure 8c**). The thickest average under-ice layers were observed on the first observation date (July 14), then gradually thinned such that none were observed on survey lines by the final date of observations. False bottoms had an average thickness of 0.06–0.11 m (**Figure 8b**). Thinning occurred rapidly, such that there were no false bottoms observed by the end of July.

False bottoms were observed at the FYI coring site July 6–29 (denoted by the x's in **Figure 8b**). The average thickness increased over July 6, 13, and 20 (with 6, 9, and 13 measurements on each date, respectively), and decreased on July 29 (15 measurements) (Table S1). A number of locations at the coring site were observed to have multiple false bottoms on July 20 and 29. These observations have been excluded from the averages presented here, but provide evidence that multiple false bottoms can form, likely from temporal increase in FWE such as associated with
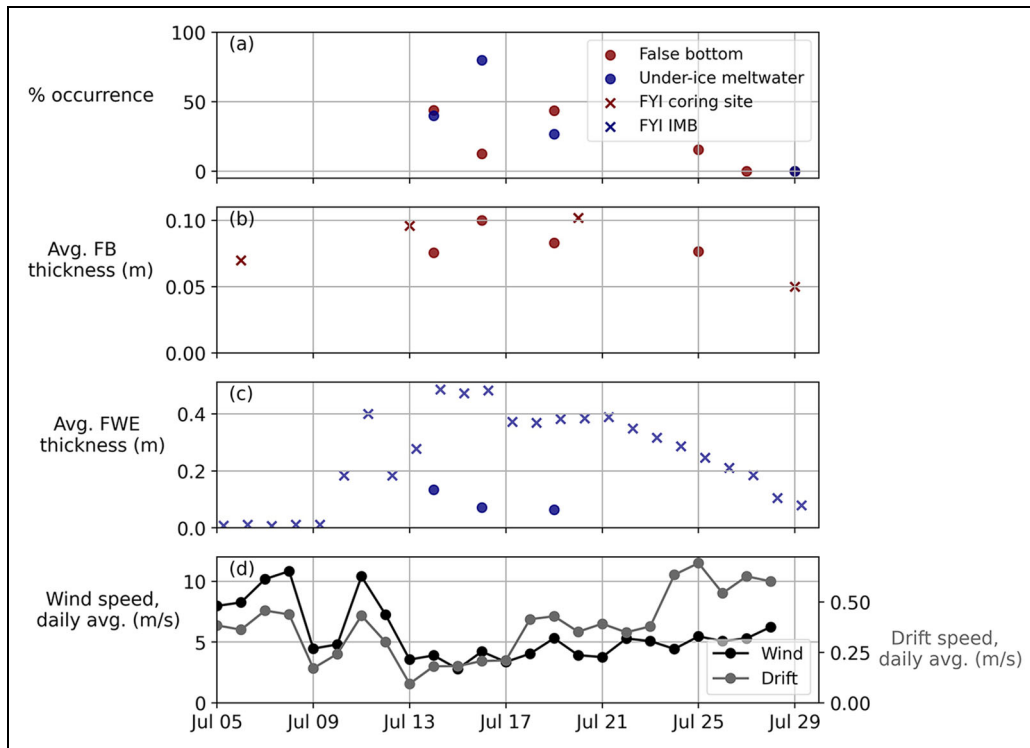
Figure 8. Time series characterizing observed features and factors relating to their occurrence. Percent occurrence of (a) false bottoms (dark red) and under-ice meltwater layers (blue), average thickness of (b) false bottoms (FB) and (c) freshwater equivalent (FWE) of under-ice meltwater layers where observed, and (d) daily average wind speed (black) and drift speed (grey). The x's in (b) and (c) correspond to observations from the first-year ice (FYI) coring site and ice mass balance (IMB) site, respectively. Circles in (a)-(c) indicate observations along survey lines.

pond drainage events. The FYI IMB, which was nearby but not exactly collocated with the FYI coring site (**Figure 2**), shows evidence of an under-ice meltwater layer beginning on July 10 and increasing in thickness through July 16. It declines steadily from July 21 to July 29. Note that the under-ice meltwater thicknesses inferred from the IMB are substantially larger than those from the survey lines, which had a maximum thickness of 0.16 m. It is possible that the IMB was in a thicker under-ice meltwater layer than other observations, as it was located more towards the interior of the floe, or that the thickness of the under-ice meltwater layer could be somewhat overestimated by the methodology. The formation of false bottoms at IMB locations is not discernible due to the lack of an associated temperature signal, and no drilling was undertaken at these sites. Based on the observation of false bottoms in close proximity to the IMB, false bottoms were likely present at some point.

Time series of daily average wind and drift speed (**Figure 8d**) provide insight into the drivers of temporal evolution. The first observations of under-ice features occurred just after a drop in the wind and drift speeds, dampening potential mixing and allowing the meltwater input to accumulate and form stratified fresher layers and false bottoms. The drift speed gradually increased over July 13–25, which likely led to a higher friction velocity that ultimately eroded false bottoms and under-ice meltwater layers.

Meltwater from snow and ice melt likely finds its way into under-ice meltwater layers either by drainage from the sea ice surface, where meltwater often accumulates in melt ponds, or directly as from sea ice basal melt. The average total freshwater input from snow and sea ice melt over June 25 to July 30 was 77 cm. The daily average freshwater input over the period of observations presented here (July 5–29) was typically 1–3 cm/day, with ice surface melt contributing over 80% (Raphael et al., 2022). This estimate excludes contributions from lateral melt, which drains directly into leads. Pond drainage events and the resultant input of relatively fresh meltwater likely contributed to the formation and persistence of under-ice meltwater layers and false bottoms, while a reduction in pond drainage events may have contributed to their demise by removing a substantial meltwater source. Areal pond coverage on three dates in July is demonstrated by snapshots from SkySat Planet scenes (Planet Labs, Inc; Wright et al., 2021) of the MOSAiC floe (**Figure 9**). In general, higher pond coverage was observed along Line 3. Drawing any conclusions about the spatial correspondence of melt ponds and under-ice meltwater layers from these observations is challenging due to the temporal mismatch in observations.

While both pond growth and drainage can be observed over most areas of the floe, the images show that pond behavior is heterogeneous and the timing and magnitude of meltwater flux varies substantially around the floe
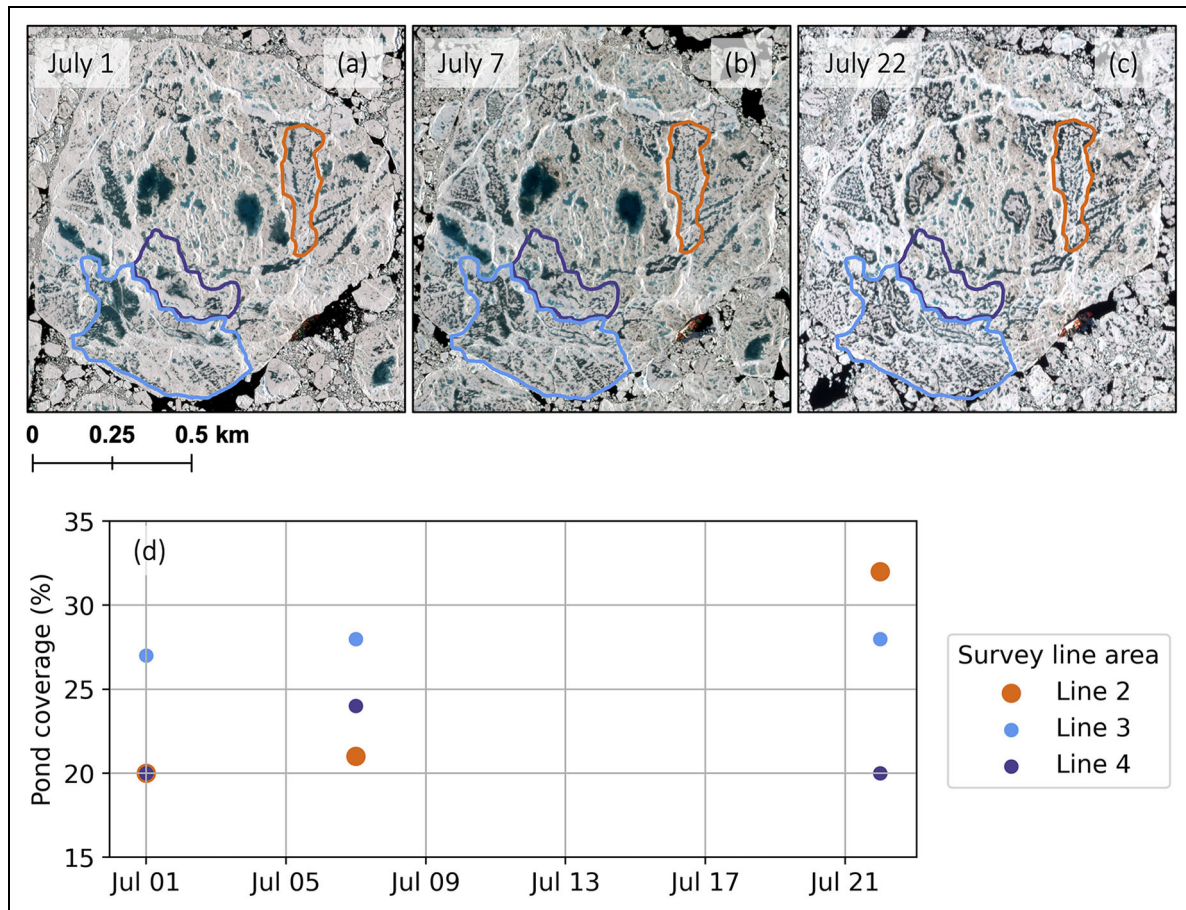
Figure 9. Melt pond evolution over the period of under-ice meltwater and false bottom evolution. SkySat Planet satellite images (Planet Labs, Inc) on (a) July 1, (b) July 7, and (c) July 22 show changes in pond coverage. (d) The time evolution of percent pond coverage is calculated for the areas outlined in the images, which approximately correspond to the drainage areas of Line 2 (orange), Line 3 (blue), and Line 4 (purple) (**Figure 2**).

(Webster et al., 2022). The initial formation of false bottoms coincides with observations of surface melt pond drainage; the first recorded observations of false bottoms on the MOSAiC floe were at the FYI coring site on July 6, when there was visible reduction in the extent of large ponds nearby (light blue outline in **Figure 9**). Additionally, the initial measurement of false bottom formation at mass balance stakes in the area adjacent to Lines 0 and 1 occurred directly after a large input of meltwater to the ocean associated with a significant vertical pond drainage event July 11–13. There is a substantial reduction in the pond coverage over the area around Line 4 (purple outline in **Figure 9**), which also included the FYI IMB (blue x's in **Figure 8c**), following July 7. This reduction coincides with the increase in equivalent freshwater thickness of the FYI IMB site, from July 9 to July 16, likely due to substantial meltwater input from pond drainage. In fact, observations from the floe indicated substantial drainage in the area near the FYI coring site from July 11 to July 13 (Webster et al., 2022). Conversely, a substantial increase in the pond coverage over the area surrounding Line 2 coincides with the reduction in under-ice meltwater observations (**Figure 8a**), possibly indicating the impact of a reduction in

meltwater input. By this time, drainage had been observed at most ponds.

3.3. Composition of under-ice meltwater and false bottoms

Figure 10 shows the salinity and $\delta^{18}O$ values from samples collected along the survey line on July 25 (Lange et al., 2022). (Complete profiles are shown in Figure S10.) Characteristic endmember values for snow and FYI (grey- and blue-shaded regions) are derived from samples taken over July (Lange et al., n.d.). Snow samples from summer are characterized by $\delta^{18}O$ ratio of −19.1 ± 9.8‰ (mean ± 1 standard deviation) and salinity of 0, which agrees rather well with the snow values observed by Tian et al. (2018) in the Beaufort Sea in late fall. FYI sea ice samples are characterized by $\delta^{18}O$ ratio of −0.39 ± 0.47‰ with salinities of 2.4 ± 0.3 (Lange et al., n.d.). We used the most saline seawater measured beneath the false bottom as the seawater endmember, as this value likely represents the water the meltwater mixes with below the ice. These seawater values are similar to those found by Tian et al. (2018). Grey dashed lines provide reference of mixing lines between these three endmembers.
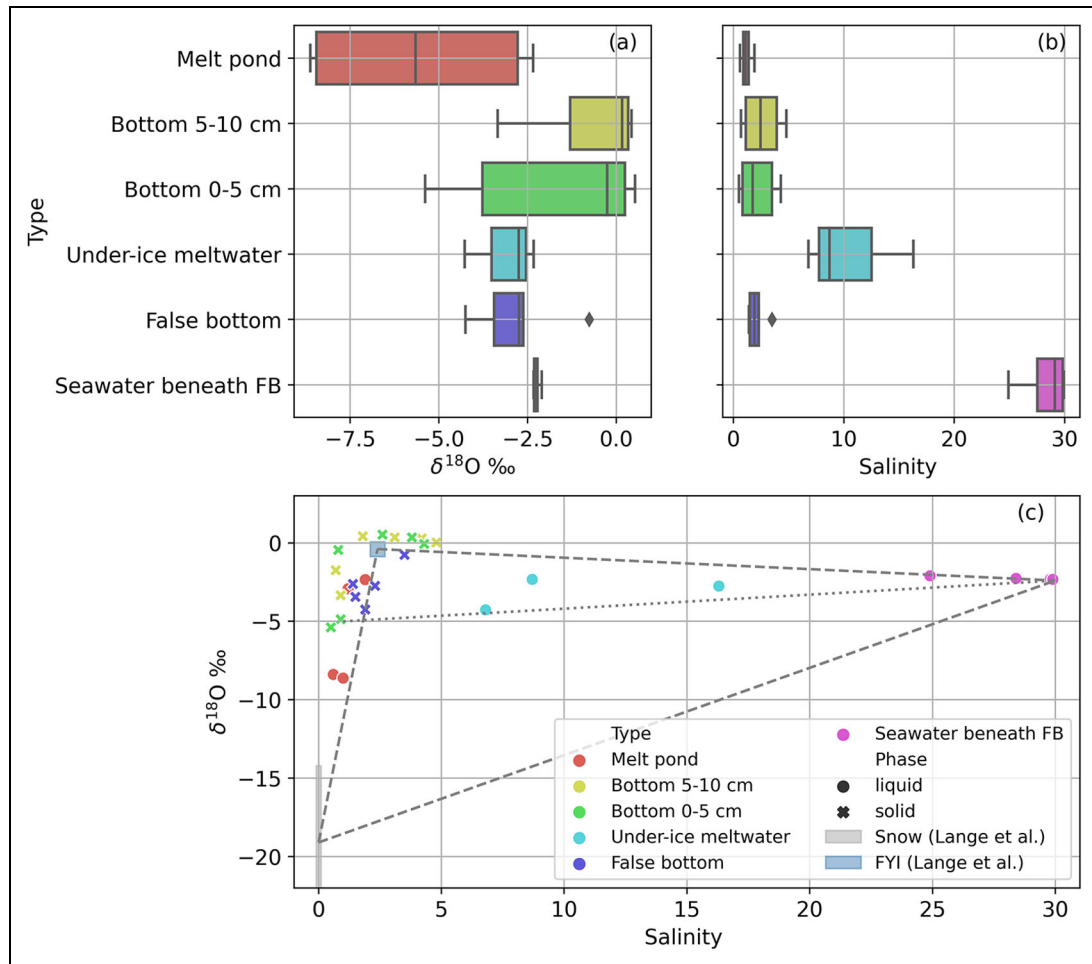
Figure 10. Composition analysis from $\delta^{18}O$ isotope and salinity sampling along survey lines. The ranges of $\delta^{18}O$ and salinity for each component are summarized as box and whisker plots in (a) and (b), respectively, and all individual points are shown in salinity-$\delta^{18}O$ space in (c). Grey- and blue-shaded areas represent endmember values for snow and FYI from Lange et al. (n.d.), and grey dashed lines are mixing lines between endmembers.

Melt pond samples have a range of salinity and $\delta^{18}O$ values along the mixing line between FYI and snow endmembers, indicating contributions from precipitation (snow) and sea ice melt. There is little indication of seawater intrusion from pond connection with the ocean below (due either to natural processes or sampling efforts) in the sampled ponds. Under-ice meltwater layer samples fall along the mixing line between melt ponds and seawater (grey dotted line), suggesting 52–81% contribution from surface melt ponds. With an average salinity of 10.6 and $\delta^{18}O$ of −3.1‰, we applied the 3-component model of Östlund and Hut (1984) to determine the relative fractions of melted FYI, snow, and seawater, using the endmember values defined above. The results suggest that the under-ice meltwater layer was approximately 58% FYI melt, 11% snow, and 31% seawater. For the average FWE thickness of 0.08 m, these values correspond to 0.04 m of FYI melt and 0.01 m snow water equivalent.

Results from the bottom of ice cores show the influence of under-ice meltwater on FYI, in agreement with earlier results of Eicken (1994) from Arctic multiyear ice. While ice 5–10 cm above the bottom corresponds to

typical FYI values (in terms of both salinity and $\delta^{18}O$), the more negative $\delta^{18}O$ values at the bottom 0–5 cm of some FYI cores indicate that under-ice meltwater, including a mix of snow and seawater, was incorporated by diffusional transport into the very bottom segment (either from flushing or directly from the meltwater layer). The incorporation of under-ice meltwater into the ice explains the slightly lower $\delta^{18}O$ observed at the very bottom of some FYI ice cores.

False bottoms typically form at the interface of under-ice meltwater layers with seawater. The low salinity of false bottoms indicates that they likely result primarily from freezing meltwater. Additionally, the low $\delta^{18}O$ values of false bottoms (in general agreement with the values observed in Eicken (1994) are similar to those in the under-ice meltwater layers, suggesting a significant contribution from the meltwater rather than from seawater below. However, the fractionation of oxygen isotopes during freezing can enrich the isotope occurrence in ice relative to the water from which it froze; values around 2‰ are typical for natural sea ice, but can approach zero during rapid freezing (e.g., O'Neil, 1968; Lehmann and

Siegenthaler, 1991). Our few seawater samples and FYI values indicate fractionation of this magnitude during FYI formation, which was also the case for FYI previously sampled in the Nansen basin (Granskog et al., 2017). The uncertainty in the fractionation values here make it difficult to determine with confidence the relative contributions from meltwater and seawater to false bottom composition. If we assume sufficiently rapid growth that the effect of fractionation was negligible, the false bottom can be estimated to be formed nearly completely from the meltwater layer, while more typical fractionation values would suggest seawater contributions greater than 50%. Taking the average false bottom salinity of 2.1 and $\delta^{18}O$ of $-2.8‰$, we applied the 3-component model (Östlund and Hut, 1984) to determine the relative fractions of melted FYI, snow, and seawater of false bottom as approximately: 87% FYI melt, 13% snow, and <1% seawater. Notably, assuming a typical isotopic fractionation rate of sea ice (2‰) only increases the relative fraction of seawater by 1%, but nearly doubles the relative contribution from snow. Additionally, the given average salinity of 2.1 and near-freezing temperatures suggest a brine volume of approximately 5% which could be considered semipermeable, in contrast to the less permeable layer (with salinity of approximately 1) measured by Eicken (1994).

These samples were collected relatively late in the summer, after significant pond drainage and ocean mixing had begun to increase (**Figure 8**). Future work should target the temporal evolution of these characteristics, if possible using less destructive sampling methods. This approach would allow better characterization of the relative role of under-ice melt and melt pond drainage as constituents in under-ice meltwater layer formation, in order to better understand the implications for the ice and ocean system.

3.4. Simulation with a 1D model

Notz et al. (2003) presented a model for false bottom growth and evolution due to diffusional transport of heat and salt. The model additionally allows for turbulent heat and salt fluxes based on far field ocean properties. Here, we applied this model to false bottom evolution observed at the FYI coring site (the x's in **Figure 8b**), where false bottom growth and dissolution were observed at four points in time throughout the month of July, to better understand the evolution of false bottoms and likely forcing conditions.

The model is forced with observed values driving diffusional and turbulent fluxes to the extent possible. Ice (false bottom) bulk salinity, S_i, is defined as 2.1 based on an average from coring activities. Surface temperature, T_s, which in the case of the false bottom refers to the temperature of the void space water, is defined as -0.7 °C based on YSI measurements on July 25. Far field temperature and salinity (T_{inf} and S_{inf}) are obtained from the deepest measurements in under-ice profiles made with the YSI probe on available days (July 13, 16, 19, 29), and are interpolated linearly (**Figure 11a**). YSI measurements were not available for July 6, so earliest observations (from July 13) are used over this period. Observations of ice-ocean friction velocities (u_*) are not available, and so were

estimated based on the daily-averaged ice drift velocity (**Figure 8d**), which was assumed to represent the relative ice-ocean velocity, u_{rel}, as:

$$u_*^2 = c_{d,io} \times u_{rel}^2 \qquad (2)$$

Two different values of the ice-ocean drag coefficient $c_{d,io}$ were used. The first was estimated by iterating with the model to find the "best fit" to obtain the observed change in false bottom thickness from July 13 to July 20 ($c_{d,io} = 2.5 \times 10^{-7}$). A low friction velocity needed to reproduce the observed changes could also be achieved by a reduction in local relative ice-ocean velocity, as discussed below. The second is a more typical Arctic ice-ocean drag coefficient (2.5×10^{-3}; Cole et al., 2017, characteristic for what was observed at the MOSAiC floe during the winter.

The observed evolution of false bottom thickness is compared with model predictions using two drag coefficients in **Figure 11c**. The drag coefficient that best matches the observed changes in false bottom thickness July 13–20 is exceptionally low. No changes to other parameters within a reasonable range of values (Notz et al., 2003) reproduced the observed false bottom thickness without a substantial reduction to the ice-ocean drag coefficient. The low drag coefficient required to reproduce observed changes could possibly be a result of under-ice meltwater layers (and other meltwater stratification) resulting in "slippery layers" reducing under-ice drag. Additionally, the actual relative ice-ocean velocity at the location of false bottom formation could be significantly lower than that estimated by drift speed, in part due to the sheltering by under-ice topography which helps to protect and maintain these slippery layers essentially decoupled from the ocean below. Notably, none of the model settings tested captured the false bottom thinning observed between July 20 and July 29. Rather, growth is predicted to increase around July 19, when the far field temperature increased. As the floe neared the ice edge, warmer subsurface ocean temperatures and possible solar heat inputs to meltwater layers likely impacted the overall ice mass balance, and melt was observed to increase all across the floe. The 1D model is not equipped to capture these processes. Notz et al. (2003) were similarly unable to predict false bottom disappearance in prior observations associated with storm-induced mixing and presumably enhanced salt flux.

Overall, these model results demonstrate that a low ice-ocean friction velocity is likely at slippery meltwater layers beneath the sea ice as a combination of a low drag coefficient and reduced local relative ice-ocean velocities. This finding is consistent with prior work indicating that ephemeral meltwater layers can effectively decouple the ice and the ocean below (Gallaher et al., 2016; Cole et al., 2017). Additionally, we observed that the evolution of the false bottom is sensitive to the ice-ocean friction velocity. This sensitivity suggests that more measurements of this property during the summer season when under-ice meltwater layers occur are needed to understand variability in ice-ocean momentum transfer. The formulation of the Notz et al. (2003) model is not intended to simulate initial formation or full melt, which limits its application to
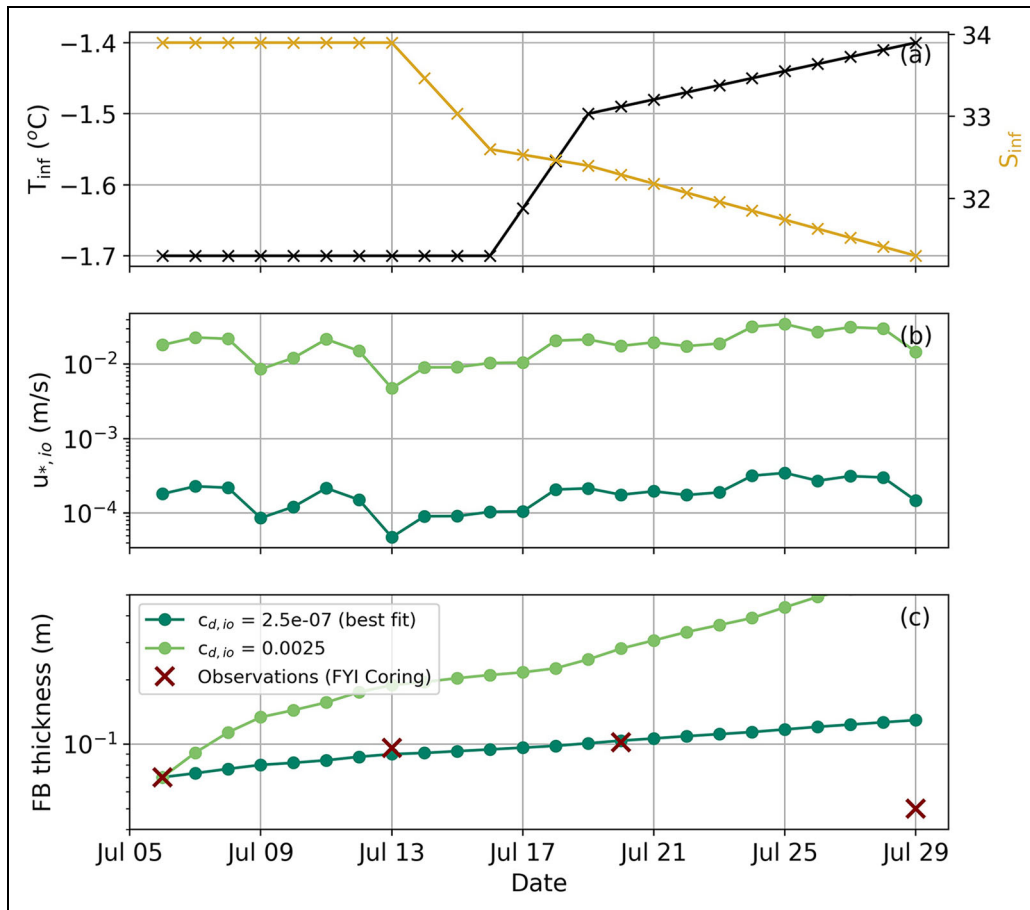
Figure 11. One-dimensional growth and evolution model predictions at the FYI coring site, July 6–29, 2020.
We used the Notz et al. (2003) model, forced with observationally-based estimates of (a) far field temperature (black) and salinity (gold), and (b) ice-ocean friction velocity for two drag coefficients (Equation 2). (c) Modeled false bottom thickness (green), with shades corresponding to friction velocities in (b) are compared with average observed thickness (dark red).

larger scales, requiring parameterization in other manners. As a first step, a basin-scale false bottom parameterization could be based on the fraction of 1–1.5 m ice with some ridged fraction, volume and timing of melt pond drainage, and on low ice-ocean friction velocities which could possibly be implied by low wind and drift velocities.

3.5. Comparison with prior observations
Overall, our observations contained false bottoms in about 20% of observations throughout July, which compares well with prior campaigns. Evidence of false bottoms was seen in about 10% of observations during a campaign in the Beaufort Sea in the early 1990s (Jeffries et al., 1995). They were seen in about 15% of observations during the SHEBA field campaign (Perovich et al., 2003), which took place on multiyear ice in the Chukchi Sea and had approximately half as much cumulative freshwater melt input as that observed on MOSAiC by July 30. We hesitate to draw conclusions about temporal evolution in false bottom frequency in comparing these observational datasets due to the differences in location and primary ice types, but note that the topography of FYI and higher cumulative meltwater input on MOSAiC are likely more conducive to higher prevalence of false bottom growth. Nonetheless,

a moderate prevalence seems to be consistent across the basin regardless of ice type or decade.

In some prior observations, the false bottoms also did not persist into fall (Perovich et al., 2003), while in others they were believed to persist until fall freeze-up such that the prevalence would likely be consistent from the maximum onwards. Evidence of the formation of under-ice meltwater layers and their persistence into winter has been reported from one third of the multiyear ice cores sampled during spring in the Lincoln Sea from 2010–2013 (N = 16) based on $\delta 18O$ isotope composition (Lange et al., 2021).

The dissolution and thinning of false bottoms on MOSAiC with increased drift rates as the floe neared the ice edge may skew the comparison of overall percentages; in fact, these features may have occurred at higher prevalence than in prior observations, but were overall less persistent than in some earlier campaigns. The maximum occurrence rate in our observations on a single day was around 44%. The higher prevalence could be due to the mixture of FYI and SYI in the study floe, which allowed meltwater to become trapped under level ice near ridges, whereas prior campaigns were primarily observing MYI. Prior observations, as well as those presented here, may

suffer from sampling bias based on where features of interest were first observed. Without more extensive observations of these features, concluding with certainty what factors led to the high maximum occurrence or if this occurrence is indicative of a basin-wide trend is not possible.

3.6. Impacts on the ice mass balance

The presence of under-ice meltwater and formation of false bottoms play a role in the evolution of the Arctic ice-ocean system. The sea ice mass balance is impacted by the reduction of heat flux from the ocean to the ice bottom, due to the isolating effect of the under-ice meltwater layers and the associated ice growth. Comparisons of melt rates at mass balance stake sites with and without false bottoms present indicate that the overall impact on mass balance of the main ice pack is small (Raphael et al., 2022) compared to the nearly 0.5-m difference in basal melt suggested in prior observations (Provost et al., 2019). There appears to be a minor reduction in bottom melt during the period when false bottoms were present, which amounts to a small (approximately 0.04 m) reduction in cumulative melt over the melt season. Similar magnitudes of reduction in ice melt were suggested by a modeling study (Smith, 2019), where smaller changes were predicted under thinner ice. The difference was not larger because ice melt does not fully stall in the presence of false bottoms, as ablation of the ice bottom can still occur due to solar heating of meltwater layers. This effect was evident at the FYI coring site during MOSAiC, where the sea ice pack was thinning even as the false bottom was growing. The biggest impact on the mass balance is a positive contribution from the false bottom itself, which has been observed to remain into fall freeze-up in prior studies (e.g., Eicken et al., 2002).

Other important impacts of the meltwater layer and false bottoms include their effects on under-ice species. Observations indicated that the meltwater negatively impacted the occurrence of under-ice diatoms (*Melosira arctica*), which were no longer present within a week of the accumulation of meltwater under the ice (Figure S1). Such effects will be addressed in depth in future studies.

4. Conclusions

Under-ice meltwater layers and false bottoms were observed to occur in approximately 20% of measurements during MOSAiC surveys targeting these features, but their distribution varied significantly both spatially and temporally. Their occurrence appears to be a result of the convergence of a few key factors, and the analysis suggests the following conclusions:

- Spatially, these features are most prevalent on relatively thin, level ice with proximal ridges on at least two sides. Proximity of ridges is a necessary but not sufficient condition, as it does not fully explain spatial variability. Future measurements of under-ice topography in areas where under-ice meltwater layers and false bottom observations

are made will help illuminate controls on spatial variability.
- Temporally, these features occur during periods of substantial meltwater input (early to mid-summer) and when ice-ocean friction velocity is low.
- Isotope analysis suggests that the sampled false bottom largely formed from freezing of the under-ice meltwater layer, while the sampled meltwater layer sampled consisted of a mix of ice melt (58%), seawater (31%), and snow melt (11%). The compositions of these features might have evolved over the period of melt.
- The processes driving false bottom growth are sufficiently well understood such that it can generally be captured in a 1D model (Notz et al., 2003), but the high sensitivity to forcing is limiting. Comparisons indicate that the ice-ocean friction velocity, which is particularly difficult to capture and constrain, was likely exceptionally low as a result of a combination of low relative velocities in sheltered under-ice meltwater layers and low ice-ocean drag coefficient. This finding motivates more work to understand the range of values during the summer and the impact of slippery meltwater layers.
- The frequency of false bottoms observed during MOSAiC was similar to or somewhat higher than prior observations. These comparisons do not necessarily indicate temporal trends of prevalence, but could suggest increased frequency on first-year ice and that both features are likely common across the Arctic basin.
- While a small reduction in cumulative melt of pack ice appears to take place in the presence of false bottoms, the largest impact on the mass balance is from the formation of the false bottom itself by contributing a relative increase in the sea ice volume. As the formation of both false bottoms and under-ice meltwater layers are likely to reduce the transfer of momentum, heat, and gases, further study of these features can inform our understanding of the coupled ocean-ice-atmosphere system.

Data accessibility statement

All data sets used herein are publicly available at the archives as listed:

- MOSAiC drill line surveys and near-surface ocean temperature and salinity are archived in the National Science Foundation's Arctic Data Center (Smith et al., 2021a; Smith et al., 2021b): https://doi.org/10.18739/A2707WP92 and https://doi.org/10.18739/A2TT4FV1G.
- MOSAiC wind data: Schmithüsen (2021): Continuous meteorological surface measurement during POLARSTERN cruise PS122/4. Alfred Wegener Institute, Helmholtz Centre for Polar and Marine

Research, Bremerhaven, PANGAEA, https://doi.org/10.1594/PANGAEA.935224.

- MOSAiC drift data: Archived at Rex (2021).
- SkySat Imagery of Planet Labs, Inc. was analyzed and made available through: Wright et al. (2021). Melt Pond Maps around the Multidisciplinary drifting Observatory for the Study of Arctic Climate (MOSAiC) Drifting Station derived from High Resolution Optical Imagery, 2020. urn: node: ARCTIC. doi:10.18739/A2696ZZ9W.
- Autonomous SIMBA measurements at FYI (2019T66) are available at https://doi.pangaea.de/10.1594/PANGAEA.938134 (Lei et al., 2021).
- Airborne laser scanner (ALS) survey data used here are archived at Hutter et al. (2021).
- Salinity and δ^{18}O analysis from dedicated cores and snow and sea ice samples used as reference here are being archived at Pangaea (Lange et al., 2022).

Supplemental files

The supplemental files for this article can be found as follows:

Video S1. GoPro video through the ice on Survey Line 4, July 25 14:24 UTC.

Video S2. GoPro video through the ice on Survey Line 3, July 25 16:24 UTC.

Video S3. GoPro video through the ice on Survey Line 3, July 25 17: 20 UTC.

Video S4. GoPro video through the ice on Survey Line 5, July 27 18:26 UTC.

Figure S1. Still images from GoPro videos taken near the FYI coring site.

Figure S2. Topography from drill line survey along Line 0 on July 14.

Figure S3. Topography from drill line survey along Line 0 on July 16.

Figure S4. Topography from drill line survey along Line 1 on July 16.

Figure S5. Topography from drill line survey along Line 2 on July 19.

Figure S6. Topography from drill line survey along Line 3 on July 25.

Figure S7. Topography from drill line survey along Line 4 on July 25.

Figure S8. Topography from drill line survey along Line 5 on July 27.

Figure S9. Topography from drill line survey along Line 5 on July 29.

Figure S10. Profiles of δ^{18}O (left) and salinity (right).

Table S1. Summary of observations of false bottoms at the FYI coring site.

Acknowledgments

Funding

Competing interests

The authors declare that they have no conflict of interest.

Author contributions

Contributed to conception and design: MS, IR, LvA, BAL, IM, AF.

Contributed to acquisition of data: MS, IR, LvA, BAL, IM, ES, MW, AF, RL.

Contributed to analysis and interpretation of data: MS, LvA, BAL, MAG, MW, IR.

Drafted and/or revised the article: MS drafted the first version of the manuscript, and all authors contributed to writing and revisions.

Approved the submitted version for publication: All authors.

References

Alexandrov, D, **Nizovtseva, I**. 2008. To the theory of underwater ice evolution, or nonlinear dynamics of "false bottoms." *International Journal of Heat and Mass Transfer* **51**(21–22): 5204–5208.

Cole, ST, **Toole, JM**, **Lele, R**, **Timmermans, ML**, **Gallaher, SG**, **Stanton, TP**, **Shaw, WJ**, **Hwang, B**, **Maksym, T**,

Wilkinson, JP, Ortiz, M, Graber, H, Rainville, L, Petty, AA, Farrell, SL, Richter-Menge, JA, Haas, C. 2017. Ice and ocean velocity in the Arctic marginal ice zone: Ice roughness and momentum transfer. *Elementa: Science of the Anthropocene* **5**: 55. DOI: http://dx.doi.org/10.1525/elementa.241.

Eicken, H. 1994. Structure of under-ice melt ponds in the central arctic and their effect on, the sea-ice cover. *Limnology and Oceanography* **39**(3): 682–693.

Eicken, H, Krouse, H, Kadko, D, Perovich, D. 2002. Tracer studies of pathways and rates of meltwater transport through Arctic summer sea ice. *Journal of Geophysical Research: Oceans* **107**(C10): SHE–22.

Gallaher, SG, Stanton, TP, Shaw, WJ, Cole, ST, Toole, JM, Wilkinson, JP, Maksym, T, Hwang, B. 2016. Evolution of a Canada Basin ice-ocean boundary layer and mixed layer across a developing thermodynamically forced marginal ice zone. *Journal of Geophysical Research: Oceans* **121**(8): 6223–6250. DOI: http://dx.doi.org/10.1002/2016JC011778.

Gradinger, R. 1996. Occurrence of an algal bloom under Arctic pack ice. *Marine Ecology Progress Series* **131**: 301–305.

Gradinger, R. 1999. Vertical fine structure of the biomass and composition of algal communities in Arctic pack ice. *Marine Biology* **133**(4): 745–754.

Granskog, MA. 2021. Overview sea ice cores collected by the snow and sea ice physics (ICE) team on the multidisciplinary drifting observatory for the Study of Arctic climate (MOSAiC) expedition. *Zenodo* **10**(1): 000046. DOI: http://dx.doi.org/10.5281/zenodo.4719905.

Granskog, MA, Rösel, A, Dodd, PA, Divine, D, Gerland, S, Martma, T, Leng, MJ. 2017. Snow contribution to first-year and second-year Arctic sea ice mass balance north of Svalbard. *Journal of Geophysical Research: Oceans* **122**(3): 2539–2549.

Hanson, AM. 1965. Studies of the mass budget of Arctic pack-ice floes. *Journal of Glaciology* **5**(41): 701–709.

Hutter, N, Hendricks, S, Jutila, A, Ricker, R, von Albedyll, L, Birnbaum, G, Haas, C. 2021. Gridded airborne laserscanner (ALS) elevation data (L4) for three flights during MOSAiC (prerelease). *Zenodo* DOI: http://dx.doi.org/10.5281/zenodo.5121824.

Jeffries, M, Schwartz, K, Morris, K, Veazey, A, Krouse, H, Gushing, S. 1995. Evidence for platelet ice accretion in Arctic sea ice development. *Journal of Geophysical Research: Oceans* **100**(C6): 10905–10914.

Lange, BA, Granskog, MA, Meyer, H, Bauch, D, Smith, MM, von Albedyll, L, Raphael, I, Matero, I, Salganik, E. 2022. Oxygen and hydrogen isotopic ratios from sea ice bottom, false bottom ice, under-ice meltwater layer and surface melt pond samples collected during MOSAiC leg 4 (PS122.4). *PANGAEA*. DOI: https://doi.pangaea.de/10.1594/PANGAEA.943734.

Lange, BA, Haas, C, Mucci, A, Beckers, JF, Casey, JA, Duerksen, S, Granskog, MA, Hatam, I, Niemi, A, Reppchen, A, Michel, C. 2021. Contribution of snow to Arctic first-year and multi-year sea ice mass balance within the last ice area. *Journal of Geophysical Research: Oceans* **126**(5): e2020JC016971.

Lange, BA, Michel, C, Beckers, JF, Casey, JA, Flores, H, Hatam, I, Meisterhans, G, Niemi, A, Haas, C. 2015. Comparing springtime ice-algal chlorophyll *a* and physical properties of multi-year and first-year sea ice from the Lincoln Sea. *PLoS One* **10**(4): e0122418.

Lange, BA, Salganik, E, Macfarlane, A, Schneebeli, M, Høyland, K, Gardner, J, Müller, O, Divine, DV, Kohlbach, D, Katlein, C, Granskog, M. n.d. Snowmelt contributes to first-year ice ridge consolidation during summer melt. *Elementa Science of the Anthropocene*, under review in Elementa.

Lehmann, M, Siegenthaler, U. 1991. Equilibrium oxygen-and hydrogen-isotope fractionation between ice and water. *Journal of Glaciology* **37**(125): 23–26.

Lei, R, Cheng, B, Hoppmann, M, Zuo, G. 2021. Temperature and heating induced temperature difference measurements from the sea ice mass balance SIMBA 2019T66, deployed during MOSAiC 2019/20. *PANGAEA*. DOI: http://dx.doi.org/10.1594/PANGAEA.938134.

Lei, R, Cheng, B, Hoppmann, M, Zuo, G, Hutchings, J, Nicolaus, M, Lin, L, Zhang, F, Lan, M. n.d. Seasonal changes in Arctic sea ice mass balance and heat flux through the ice along the strengthened TDS during the MOSAiC campaign in 2019/20. *Elementa Science of the Anthropocene* **10**(1). DOI: https://doi.org/10.1525/elementa.2021.000089.

Martin, S, Kauffman, P. 1974. The evolution of under-ice melt ponds, or double diffusion at the freezing point. *Journal of Fluid Mechanics* **64**(3): 507–528.

Meyer, H, Schönicke, L, Wand, U, Hubberten, HW, Friedrichsen, H. 2000. Isotope studies of hydrogen and oxygen in ground ice-experiences with the equilibration technique. *Isotopes in Environmental and Health Studies* **36**(2): 133–149.

Nansen, F. 1902. The oceanography of the North Polar Basin, in *The Norwegian North Polar Expedition 1893−1896.* Toronto, Canada: Longmans (Scientific Results; vol. 3): 9. Available at https://www.worldcat.org/title/oceanography-of-the-north-polar-basin/oclc/8483049.

Nicolaus, M, Perovich, DK, Spreen, G, Granskog, MA, Von Albedyll, L, Angelopoulos, M, Anhaus, P, Arndt, S, Belter, HJ, Bessonov, V, Birnbaum, G, Brauchle, J, Calmer, R, Cardellach, E, Cheng, B, Clemens-Sewall, D, Dadic, R, Damm, E, de Boer, G, Demir, O, Dethloff, K, Divine, DV, Fong, AA, Fons, S, Frey, MM, Fuchs, N, Gabarró, C, Gerland, S, Goessling, HF, Gradinger, R, Haapala, J, Haas, C, Hamilton, J, Hannula, HR, Hendricks, S, Herber, A, Heuzé, C, Hoppmann, M, Høyland, KV, Huntemann, M, Hutchings, JK, Hwang, B, Itkin, P, Jacobi, HW, Jaggi, M, Jutila, A, Kaleschke, L, Katlein, C, Kolabutin, N, Krampe, D, Kristensen, SS, Krumpen, T, Kurtz, N, Lampert, A, Lange, BA, Lei, R, Light, B, Linhardt, F, Liston, GE, Loose, B, Macfarlane, AR, Mahmud, M, Matero, IO, Maus,

S, **Morgenstern, A**, **Naderpour, R**, **Nandan, V**, **Niubom, A**, **Oggier, M**, **Oppelt, N**, **Pätzold, F**, **Perron, C**, **Petrovsky, T**, **Pirazzini, R**, **Polashenski, C**, **Rabe, B**, **Raphael, IA**, **Regnery, J**, **Rex, M**, **Ricker, R**, **Riemann-Campe, K**, **Rinke, A**, **Rohde, J**, **Salganik, E**, **Scharien, RK**, **Schiller, M**, **Schneebeli, M**, **Semmling, M**, **Shimanchuk, E**, **Shupe, MD**, **Smith, MM**, **Smolyanitsky, V**, **Sokolov, V**, **Stanton, T**, **Stroeve, J**, **Thielke, L**, **Timofeeva, A**, **Tonboe, RT**, **Tavri, A**, **Tsamados, M**, **Wagner, DN**, **Watkins, D**, **Webster, M**, **Wendisch, M**. 2022. Overview of the MOSAiC expedition: Snow and sea ice. *Elementa Science of the Anthropocene* **10**(1): 000046. DOI: https://doi.org/10.1525/elementa.2021.000046.

Nixdorf, U, **Dethloff, K**, **Rex, M**, **Shupe, M**, **Sommerfeld, A**, **Perovich, DK**, **Nicolaus, M**, **Heuzé, C**, **Rabe, B**, **Loose, B**, **Damm, E**, **Gradinger, R**, **Fong, A**, **Maslowski, W**, **Rinke, A**, **Kwok, R**, **Spreen, G**, **Wendisch, M**, **Herber, A**, **Hirsekorn, M**, **Mohaupt, V**, **Frickenhaus, S**, **Immerz, A**, **Weiss-Tuider, K**, **König, B**, **Mengedoht, D**, **Regnery, J**, **Gerchow, P**, **Ransby, D**, **Krumpen, T**, **Morgenstern, A**, **Haas, C**, **Kanzow, T**, **Rack, FR**, **Saitzev, V**, **Sokolov, V**, **Makarov, A**, **Schwarze, S**, **Wunderlich, T**, **Wurr, K**, **Boetius, A**. 2021. MOSAiC extended acknowledgement. *Zenodo*. DOI: http://dx.doi.org/10.5281/zenodo.5179739.

Notz, D, **McPhee, MG**, **Worster, MG**, **Maykut, GA**, **Schlünzen, KH**, **Eicken, H**. 2003. Impact of underwater-ice evolution on Arctic summer sea ice. *Journal of Geophysical Research: Oceans* **108**(C7): 3223.

O'Neil, JR. 1968. Hydrogen and oxygen isotope fractionation between ice and water. *The Journal of Physical Chemistry* **72**(10): 3683–3684.

Östlund, HG, **Hut, G**. 1984. Arctic Ocean water mass balance from isotope data. *Journal of Geophysical Research: Oceans* **89**(C4): 6373–6381.

Perovich, D, **Smith, M**, **Light, B**, **Webster, M**. 2021. Freshwater sources and sinks for Arctic sea ice in summer. *The Cryosphere Discussions* **15**(9): 4517–4525.

Perovich, DK, **Grenfell, TC**. 1981. Laboratory studies of the optical properties of young sea ice. *Journal of Glaciology* **27**(96): 331–346.

Perovich, DK, **Grenfell, TC**, **Richter-Menge, JA**, **Light, B**, **Tucker, WB**, **Eicken, H**. 2003. Thin and thinner: Sea ice mass balance measurements during SHEBA. *Journal of Geophysical Research: Oceans* **108**(C3): 8050.

Provost, C, **Sennéchael, N**, **Sirven, J**. 2019. Contrasted summer processes in the sea ice for two neighboring floes north of 84 N: Surface and basal melt and false bottom formation. *Journal of Geophysical Research: Oceans* **124**(6): 3963–3986.

Raphael, I, **Clemens-Sewall, D**, **Perovich, D**, **Polashenski, C**, **Itkin, P**, **Regnery, J**, **Nicolaus, M**, **Jaggi, M**, **Smith, M**, **Matero, I**, **Macfarlane, A**, **Hutchings, J**, **Jutila, A**, **Fons, S**, **Oggier, M**, **Wagner, D**, **Demir, O**. 2022. Measurements of sea ice point-mass-balance using hotwire thickness

gauges and ablation stakes during the multidisciplinary drifting observatory for the study of Arctic Climate (MOSAiC) Expedition in the Central Arctic (2019-2020). *Arctic Data Center*. DOI: http://dx.doi.org/10.18739/A2NK36626.

Rex, M. 2021. *Master tracks in different resolutions of POLARSTERN cruise PS122/4, Longyearbyen - Arctic Ocean, 2020-06-04 - 2020-08-12*. Bremerhaven, PANGAEA: Alfred Wegener Institute, Helmholtz Centre for Polar and Marine Research. DOI: http://dx.doi.org/10.1594/PANGAEA.926829.

Schmithüsen, H. 2021. Continuous meteorological surface measurement during POLARSTERN cruise PS122/4: Alfred Wegener Institute, Helmholtz Centre for Polar and Marine Research, Bremerhaven. *PANGAEA*. DOI: http://dx.doi.org/10.1594/PANGAEA.935224.

Shupe, M, **Rex, M**, **Dethloff, K**, **Damm, E**, **Fong, A**, **Gradinger, R**, **Heuze, C**, **Loose, B**, **Makarov, A**, **Maslowski, W**, **Nicolaus, M**, **Perovich, D**, **Rabe, B**, **Rinke, A**, **Sokolov, V**, **Sommerfeld, A**. 2020. The MOSAiC expedition: A year drifting with the Arctic Sea ice. *Arctic Report Card*. DOI: http://dx.doi.org/10.25923/9g3v-xh92.

Skyllingstad, ED, **Paulson, CA**, **Pegau, WS**, **McPhee, MG**, **Stanton, T**. 2003. Effects of keels on ice bottom turbulence exchange. *Journal of Geophysical Research: Oceans* **108**(C12): 3372.

Smith, M, **Bozzato, D**, **Chamberlain, E**, **Dietrich, U**, **Droste, E**, **Fong, A**, **Light, B**, **Linhardt, F**, **Matero, I**, **Perovich, D**, **Raphael, I**, **Regnery, J**, **Salganik, E**, **Tavri, A**, **von Albedyll, L**, **Webster, M**. 2021a. Near-surface ocean temperature & salinity measurements (using YSI and Castaway) during the summer component of the Multidisciplinary drifting Observatory for the Study of Arctic Climate (MOSAiC) campaign in the Central Arctic Ocean, July – September 2020. *Arctic Data Center*. DOI: http://dx.doi.org/10.18739/A2TT4FV1G.

Smith, M, **Raphael, I**, **von Albedyll, L**, **Lange, B**, **Salganik, E**. 2021b. Sea ice thickness and false bottom measurements along drill lines during the Multidisciplinary drifting Observatory for the Study of Arctic Climate (MOSAiC) expedition, Leg 4. *Arctic Data Center*. DOI: https://doi.org/10.18739/A2707WP92.

Smith, N. 2019. Mathematical modelling of under-ice melt ponds and their impact on the thermohaline interaction between sea ice and the oceanic mixed layer [Ph.D. thesis]. Reading, UK: University of Reading.

Spindler, M. 1990. A comparison of Arctic and Antarctic sea ice and the effects of different properties on sea ice biota, in Bleil, U, Thiede, J eds., *Geological history of the polar oceans: Arctic versus Antarctic*. Dordrecht, The Netherlands: Kluwer Academic Publishers (NATO ASI series; vol. 308): 173–186.

Taylor, P, **Feltham, D**. 2004. A model of melt pond evolution on sea ice. *Journal of Geophysical Research: Oceans* **109**(C12): C12007.

Tian, L, **Gao, Y**, **Ackley, S**, **Stammerjohn, S**, **Maksym, T**, **Weissling, B**. 2018. Stable isotope clues to the

formation and evolution of refrozen melt ponds on Arctic sea ice. *Journal of Geophysical Research: Oceans* **123**(12): 8887–8901.

Untersteiner, N, **Badgley, FI**. 1958. Preliminary results of thermal budget studies on Arctic pack ice during summer and autumn. *Arctic Sea Ice* **598**: 85–92.

Von Albedyll, L, **Hendricks, S**, **Grodofzig, R**, **Krumpen, T**, **Arndt, S**, **Belter, HJ**, **Birnbaum, G**, **Cheng, B**, **Hoppmann, M**, **Hutchings, J**, **Itkin, P**, **Lei, R**, **Nicolaus, M**, **Ricker, R**, **Rohde, J**, **Suhrhoff, M**, **Timofeeva, A**, **Watkins, D**, **Webster, M**, **Haas, C**. 2022. Thermodynamic and dynamic contributions to seasonal Arctic sea ice thickness distributions from airborne observations. *Elementa: Science of the Anthropocene* **10**(1): 00074.

Wadhams, P. 1981. Sea-ice topography of the Arctic Ocean in the region 70 W to 25 E. *Philosophical Transactions of the Royal Society of London Series A, Mathematical and Physical Sciences* **302**(1464): 45–85

Wadhams, P. 2000. *Ice in the ocean*. Amsterdam, The Netherlands: Gordon and Breach Publishers.

Wadhams, P, **Wilkinson, JP**, **McPhail, S**. 2006. A new view of the underside of Arctic sea ice. *Geophysical Research Letters* **33**(4): L04501.

Wang, C, **Shi, L**, **Gerland, S**, **Granskog, MA**, **Renner, AH**, **Li, Z**, **Hansen, E**, **Martma, T**. 2013. Spring sea-ice evolution in Rijpfjorden (80 N), Svalbard, from in situ measurements and ice mass-balance buoy (IMB) data. *Annals of Glaciology* **54**(62): 253–260.

Webster, MA, **Holland, M**, **Wright, NC**, **Hendricks, S**, **Hutter, N**, **Itkin, P**, **Light, B**, **Linhardt, F**, **Perovich, DK**, **Raphael, IA**, **Smith, MM**, **Von Albedyll, L**, **Zhang, J**. 2022. Spatiotemporal evolution of melt ponds on Arctic sea ice: MOSAiC observations and model results. *Elementa: Science of the Anthropocene* **10**(1): 000072.

Wright, N, **Webster, M**, **Polashenski, C**. 2021. Melt pond maps around the multidisciplinary drifting observatory for the study of Arctic Climate (MOSAiC) drifting station derived from high resolution optical imagery. *Arctic Data Center*. DOI: https://dx.doi.org/10.18739/A2696ZZ9W.